Synthetic Control of Hot-Electron Thermalization Efficiency in Size-Tunable Au–Pt Hybrid Nanoparticles

Abigail M. Fagan, ^{1,†} William R. Jeffries, ^{1,†} Kenneth L. Knappenberger, Jr., ^{1,2,*} and Raymond E. Schaak ^{1,2,3,*}

ABSTRACT

Gold nanoparticles are well known to exhibit size-dependent properties that are responsible for their unique catalytic, optical, and electronic applications. However, electron-phonon coupling, which is important for photocatalysis and light-harvesting, is one of the rare properties of gold that is size-independent above a threshold value, e.g. for nanospheres larger than approximately 5 nm in diameter. Here, we show that when interfaced to a comparably sized Pt nanoparticle, the electron-phonon coupling constant of the hybrid material depends on the diameter of the Au domain. This is important because the electron-phonon coupling constant describes the efficiency by which hot electrons are converted to local heat by the primary electron-phonon scattering thermalization channel. We begin by synthesizing a library of Au-Pt hybrid nanoparticle heterodimers by growing size-tunable Au nanoparticles on Pt nanoparticle seeds. By systematically varying reagent concentration and reaction time, the Au domain diameter of the Au-Pt hybrid nanoparticle heterodimers can be tuned between 4.4 and 16 nm while the size of the Pt domain remains constant. Calibration curves allow us to dial in precise Au domain sizes, and microscopic analysis of the Au-Pt heterodimers provides insights into how they grow and how their morphologies evolve. Femtosecond time-resolved transient absorption spectroscopy reveals that for Au-Pt heterodimers having Au domain diameters of 8.7 to 14 nm, the electron-phonon coupling constant decreases by more than 80%, which is not observed for comparably sized Au nanoparticles. Interfacing smaller Au domains with Pt nanoparticle surfaces causes an increase in the density of states near the Fermi level of Au, which results in accelerated thermalization times through an increased number of electronphonon interactions. The combination of precision hybrid nanoparticle synthesis and sizedependent electron-phonon coupling may be important for designing composite metals for photocatalytic and light-harvesting applications and for engineering different functions into established materials.

KEYWORDS

nanoparticle synthesis, hybrid nanoparticles, size-tunable properties, plasmonics, hot electrons, electron dynamics, two-dimensional electronic spectroscopy

INTRODUCTION

Hybrid nanoparticles that couple together two or more distinct materials through solid-state interfaces can exhibit emergent and synergistic properties that are distinct from those of their individual components.^{1–3} For example, two-component hybrid nanoparticles that include gold can achieve simultaneous magnetic and optical imaging for theranostics⁴ and plasmon-induced

¹ Department of Chemistry, ² Materials Research Institute, and ³ Department of Chemical Engineering, The Pennsylvania State University, University Park, PA 16802

[†] These authors contributed equally

electron transfer for enhanced photocatalytic activity.^{5–7} It is possible to tune these and other properties based on the constituent materials, the number of interfaces present within the hybrid nanoparticle, and the size and shape of each domain.^{2,3} Size control of the nanoparticle domains is particularly useful in this regard because it leverages size-dependent properties while maintaining the same materials and interfaces. As an example, differences in material thickness of even one or two nanometers can significantly impact the degree of electronic coupling in core@shell nanoparticles.^{8,9} However, rigorously and precisely tuning the relative and absolute sizes of the domains within hybrid nanoparticles can be challenging. Synergistic properties that depend sensitively on the domain sizes within hybrid nanoparticles have not been extensively interrogated.

Size-dependent properties in gold-based nanoparticle systems are especially significant. The plasmon band for single component gold nanoparticles is extremely sensitive to both the size and shape of the particles. 10,11 The position of the Au plasmon peak can also be modified by coupling Au to other particles through solid-state interfaces, as has been demonstrated in the Au–Fe₃O₄, 12 Au–Ge, 13 Au–In₂O₃, 14 and Au@Pt⁸ and Pt@Au⁹ hybrid nanoparticle systems. Au nanoparticles can also exhibit size-dependent catalytic properties that can be further modified by coupling with other materials through interfaces, including for CO oxidation, $^{15-18}$ CO₂ reduction, 19 the hydrogen evolution reaction, 20 and H₂O₂ reduction. 21

A key aspect that determines the functionality of a metal nanoparticle is how efficiently the material dissipates energy. In the case of metallic gold nanoparticles, photo-excited electrons relax through a sequence of three steps. First, electron-electron scattering, which occurs over hundreds of femtoseconds, generates a hot (or athermal) electron population, establishing an elevated electron temperature. Next, these hot electrons thermalize by electron-phonon scattering on the picosecond time scale, increasing the lattice temperature. The local heat of the lattice is then dissipated to the environment in tens of picoseconds. The electron-phonon coupling constant is of heightened interested because several nanoparticle-based applications depend on the efficiency by which hot electrons are converted to local heat. In particular, the competition between hot-electron-mediated and thermally activated catalysis depends, in part, on the persistence of hot carriers. Similarly, in order for a therapeutic photodynamic therapy transducer to be effective, the rapid generation of local heat is required. Hence, the ability to tune electron-phonon scattering efficiency by tailoring nano-structure is essential to moving these and many other applications forward.

Here, we describe a synthetic strategy capable of rigorously controlling the Au domain size from 4.4 to 16 nm in Au–Pt hybrid nanoparticles and then quantify structure-specific electron-phonon scattering rates for each Au–Pt heterodimer. Notably, we leverage the unique electronic structure of Pt to demonstrate that the electron-phonon relaxation rates of the heterodimers are dependent upon the size of the gold domain, changing by a factor of approximately two (corresponding to an 80% change in the electron-phonon coupling constant) over the size range studied. These size-dependent relaxation rates for Au are exclusive to the Au–Pt hybrid nanoparticles, as these rates do not vary with size for Au nanoparticles by themselves in this range. The heterodimer system allowed us to overcome the bulk-like limits of gold electron-phonon scattering, which render the energy relaxation dynamics of Au nanospheres size independent. Taken together, the synthetic and spectroscopic results demonstrate significant domain size tunability in colloidal hybrid nanoparticles and establish a size dependence to electron-phonon coupling of Au-based nanoparticles through coupling with Pt in Au–Pt heterodimers. This combination may be significant for advancing the design of composite metals for photocatalytic and light-harvesting applications.

RESULTS AND DISCUSSION

Synthesis and Characterization of Au-Pt Heterodimers

Colloidal Au–Pt heterodimers have been synthesized previously using both aqueous^{8,9,25,26} and organic^{1,27–30} solvents. The process by which Au deposits onto the Pt seeds is believed to involve the nucleation and growth of a single, spherical domain of Au on the Pt seeds through a heterogeneous seeded growth mechanism. ^{28,29} A variety of core@shell^{8,9} and anisotropic^{26–29} morphologies have been produced, including the deposition of Au spheres^{27–29} and nanorods²⁶ on Pt nanocubes. Multiple Au domains have been grown on a single Pt seed to form clover-like heterodimers, based on the shape of the Pt seeds and the polarity of the solvent.²⁹ The size of the Au domain has been modulated by using different reaction times, over several days, at room temperature, although the Pt seeds were observed to significantly change size and shape during this process. 27 Here, we chose to synthesize Au-Pt heterodimers in organic solvents at a mildly elevated temperature, which allows us to significantly decrease the reaction time and maintain the integrity of the Pt seed particles while also rigorously controlling the Au reagent concentration and reaction time independently, which provides exquisite control over the Au domain size. Specifically, we react preformed Pt nanocube seeds with a mixture of hexanes. oleylamine, octadecene, and HAuCl₄ at 80 °C; detailed concentrations and reaction times are provided in Tables S1 and S2. Our choice of reaction conditions optimizes single-domain growth and permits rigorous control of Au domain size, rather than forming multiple domains. Reaction time and metal reagent concentration, which influence growth, are therefore our primary synthetic levers for controlling the size of the Au domain in Au-Pt heterodimers.

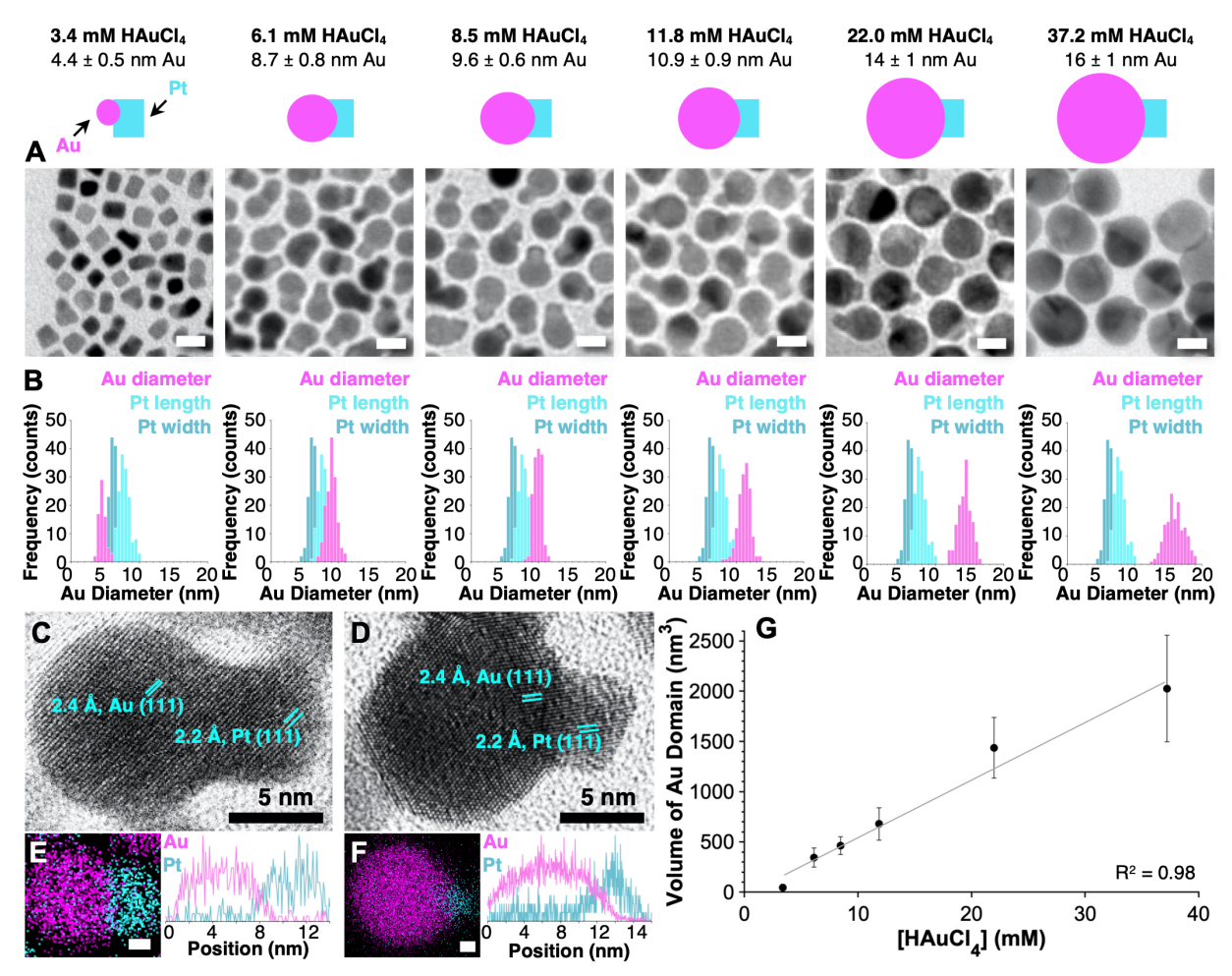


Figure 1: (A) TEM images of Au–Pt heterodimers synthesized with increasing concentration of HAuCl₄, along with illustrations (drawn to scale) of the hybrid nanoparticles. Scale bars are 10 nm. (B) Histograms showing the distribution in the measurements of the diameter of the Au domain measured parallel to the Au–Pt interface (n = 150). The same Pt length and width (corresponding to the free Pt seeds) are used for each histogram as a reference point, since the exact dimensions of the Pt domains in the heterodimers are difficult to unambiguously determine; Figure S2 shows data supporting the validity of this assumption. (C,D) HRTEM images and corresponding (E,F) STEM-EDS element maps (left) and line scans (right) of Au–Pt heterodimers having (C,E) 8.7 nm and (D,F) 14 nm Au domain sizes, respectively. Scale bars are 2 nm. (G) Plot of Au domain volume *vs.* concentration of HAuCl₄ used in each reaction. The error bars associated with the Au domain volume were obtained by error propagation calculations using the standard deviation in Au diameter measurements.

Accordingly, we began by first varying the concentration of HAuCl₄ used in the seeded growth reaction while holding the reaction time constant, building on prior work showing that increasing amounts of gold reagent available during the growth stage would lead to larger gold domain sizes. The Pt nanocube seeds, shown in the TEM image and XRD pattern in Figure S1 of the Supporting Information, are 6.1 ± 0.7 nm in width and 7.6 ± 0.8 nm in length. Figure S2 confirms that the size and morphology of the Pt seeds are retained throughout the seeded growth process. Figures 1A and 1B show TEM images and corresponding size distribution histograms of the products obtained when Pt seeds were reacted with different concentrations of HAuCl₄,

ranging from 3.4 mM to 37.2 mM, while keeping all other conditions and reagent amounts the same. For all samples, the majority product was Au–Pt heterodimers that contained one domain of Au and one domain of Pt. All HAuCl₄ concentrations facilitated heterogeneous nucleation and growth. Increasing the concentration of HAuCl₄ to the highest level used (37.2 mM) did not appear to induce homogeneous nucleation of Au; Au continues to grow on the Pt seeds. High-resolution TEM images (Figure 1C,D), STEM-EDS maps and corresponding line scans (Figure 1E,F and Figure S3), and XRD patterns (Figure S4) for representative Au–Pt heterodimers that span this range of sizes confirm the spatial segregation of the Au and Pt domains, that they are crystalline, and that they interface epitaxially, as evident by the continuous (111) fringes in the Au and Pt domains.

The size distribution histograms for the Au and Pt domains in each sample (Figure 1B) indicate that the size of the Au domain grows as the amount of HAuCl₄ increases while the size of the Pt domain remains the same as it was for the as-synthesized seed particles in Figure S1. The plot of Au domain volume (with standard deviations) vs. the amount of HAuCl₄ in Figure 1G is linear, which suggests that it can be used as a calibration curve for fine-tuning the Au domain size, which is important for interrogating size-dependent properties. The correlation between the measured Au domain diameter and calculated domain volume can be seen in Figure S5.

It is important to note one additional detail in the data shown in Figure 1. The sample having the smallest average Au domain size of 4.4 nm, made using 3.4 mM HAuCl₄, includes a significant amount (~60%) of free Pt seeds with no Au domains on them, compared to the other five Au–Pt samples in Figure 1, presumably due to the amount of Au being too low to facilitate nucleation and subsequent growth on all seed particles. While varying the amount of HAuCl₄ provides a useful synthetic lever for tuning the Au domain size, based on the calibration curve in Figure 1G, we sought to also independently investigate reaction time, using a larger amount of HAuCl₄, as a complementary parameter to tune. We chose to focus on one of the mid-range samples, the Au–Pt heterodimers made using 11.8 mM HAuCl₄, and took aliquots at various time points between 0 and 240 minutes, with the concentration remaining constant, to elucidate the time evolution of the resulting Au–Pt heterodimers.

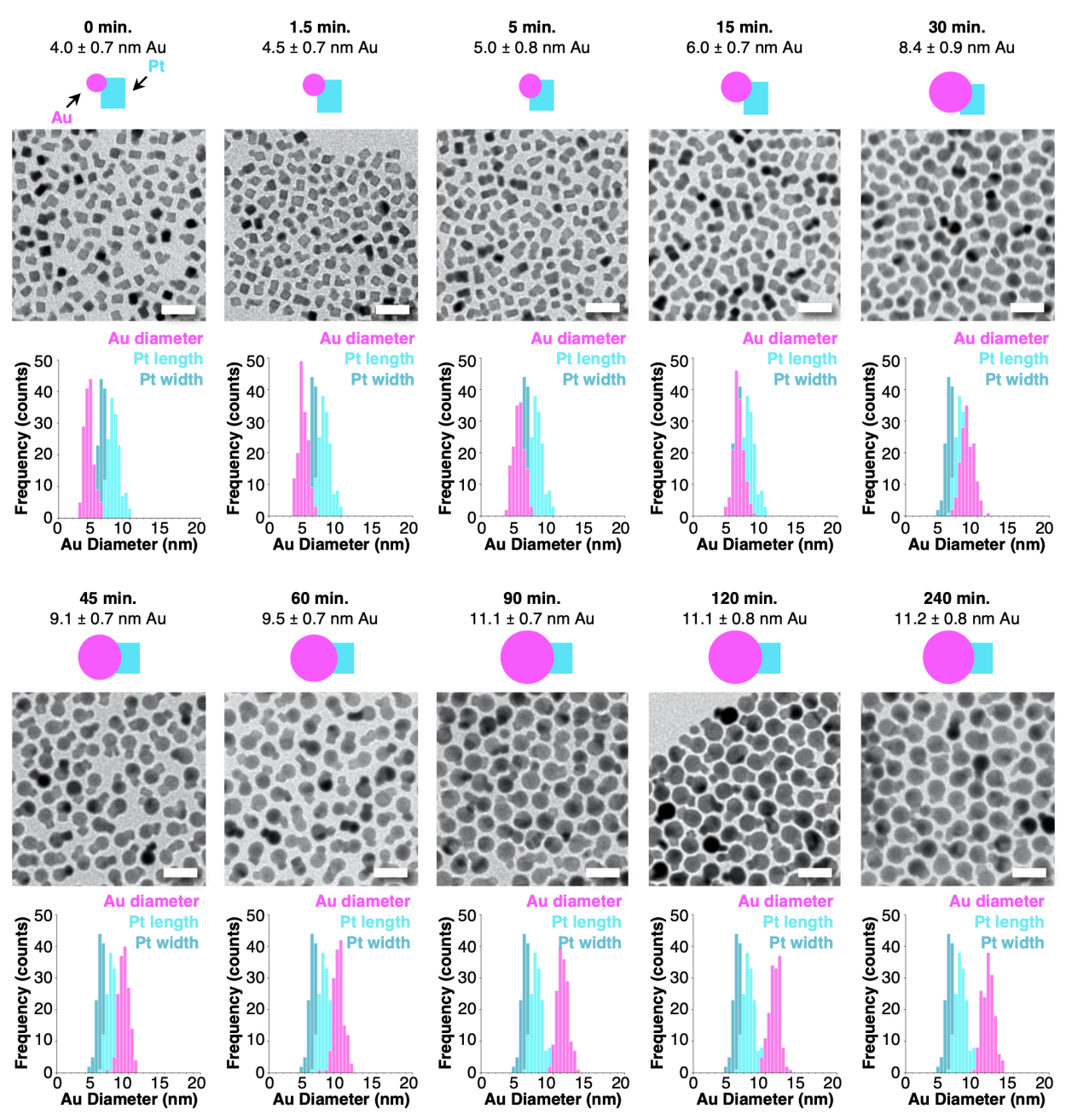


Figure 2: TEM images of Au–Pt heterodimers collected over the course of a single 4 hour reaction, with illustrations (drawn to scale) of the hybrid nanoparticles, along with the corresponding size distribution histograms (n=150). The histograms show the distribution in the measurements of the diameter of the Au domain measured parallel to the Au–Pt interface. The same Pt length and width (corresponding to the free Pt seeds) are used for each histogram as a reference point, since the exact dimensions of the Pt domains in the heterodimers are difficult to unambiguously determine; Figure S2 shows data supporting the validity of this assumption. All scale bars are 20 nm.

Figure 2 shows the TEM images for each of the aliquots noted above, along with the corresponding size distribution histograms. Figure 3A also shows a plot of Au domain volume

vs. reaction time. As expected, the Pt domain size remains constant while the Au domain size increases in size up to a reaction time of 90 minutes, with growth continuing monotonically throughout this time range. The Au domain volume increases nearly linearly with reaction time up to 90 minutes. Beyond 90 minutes, no additional growth of the Au domain occurs, presumably due to consumption of all of the HAuCl₄ that is available for growth.

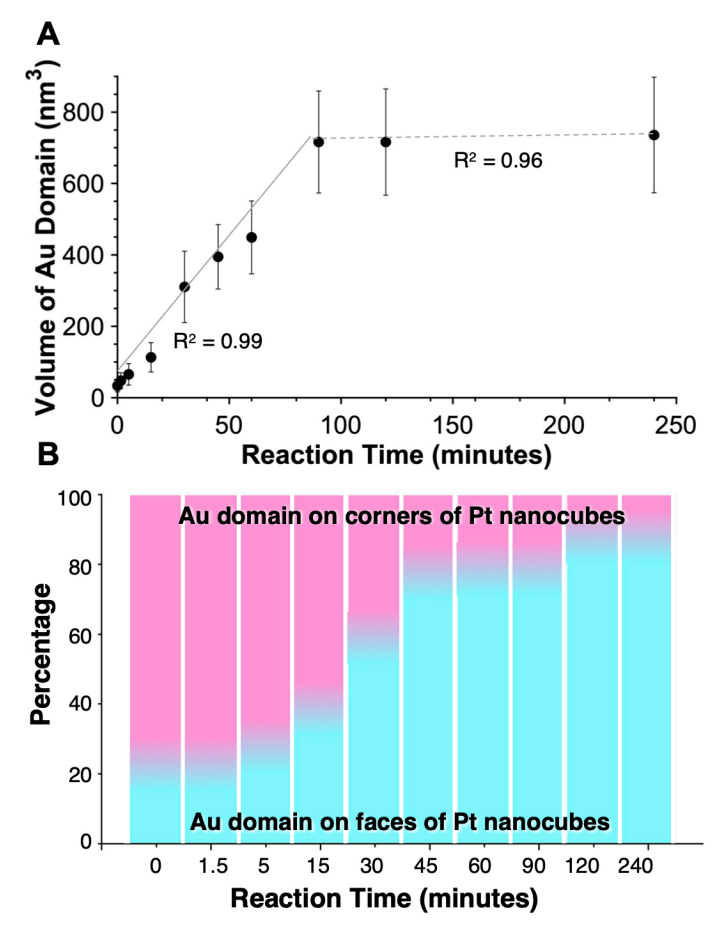


Figure 3: (A) Plot of Au domain volume *vs.* reaction time, *i.e.* the time at which each aliquot was removed. (B) Bar graph showing the approximate percentage of the sample (n = 150) of Au–Pt heterodimers where the Au domain appears to be located at the corners of the Pt seeds (top, pink) and the faces of the Pt seeds (bottom, light blue) as the reaction progresses over the course of 4 hours. The burred divisions between the corner-attached and face-attached subpopulations emphasizes that the values are approximate, as discussed in the text.

Additional insights into the growth and stability of the Au–Pt heterodimers can be gained by further analyzing the TEM images in Figure 2. At the beginning of the reaction when t = 0 min, *i.e.* the time at which the temperature reached 80 °C, TEM images suggested that small ~4 nm Au particles grew primarily on the corners of the cube-shaped Pt seeds. This behavior was also observed at 1.5 minutes. Beyond this time, as the Au domains continued to grow, there appeared to be a gradual shift from smaller Au nanoparticles preferentially attached to the corners of the cube-shaped Pt seeds to larger Au nanoparticles preferentially attached to the faces of the Pt nanocubes. The trend in these ratios is captured in the stacked bar graph in Figure 3B. It is important to note that it is difficult to unambiguously differentiate edge-attached

heterodimers from corner- and face-attached heterodimers due to their possible orientations on the TEM grid, as illustrated in Figures S6 and S7 and discussed in more detail in the Supporting Information. However, even with some uncertainty in this distribution, which is indicated by the blurred divisions between the corner- and face-attached subpopulations, the trends are still clear. As the plot in Figure 3B illustrates, the ability to finely tune the Au domain size provides useful insights into how morphology and interfaces evolve, with an apparent crossover between corner-attached and face-attached Au-on-Pt occurring when the Au domain diameter is comparable to the diameter of Pt nanocube face.

Extinction Spectra of Au–Pt Heterodimers

Extinction spectra for the Au–Pt heterodimers dispersed in toluene, as well as Au and Pt nanoparticles as controls, are shown in Figure 4; TEM images and XRD patterns for the Au and Pt nanoparticles are shown in Figures S8 and S1, respectively. The absorption features of these samples are consistent with previous descriptions of the linear extinction of Au, as well as Au@Pt and Pt@Au core@shell nanoparticles. Therefore, we provide only a brief explanation here. Pt nanocubes, by themselves, exhibit broad, featureless absorption in the range spanning 400 nm to 800 nm that increased in magnitude with decreasing wavelength, which was attributed to interband excitation. The Au–Pt heterodimers exhibit increased extinction at visible wavelengths, which was dominated by the Au-based localized surface plasmon resonance (LSPR) centered at 530 nm. The larger Au–Pt heterodimers have extinction spectra that are very similar to that of the Au nanoparticle controls, which have similar sizes as the Au domains of the Au–Pt heterodimers. The Au nanoparticle control samples having average diameters of 4.9 nm and 10 nm match very well with previously reported extinction spectra of colloidal Au nanoparticles. Ultimately, the observed trend is that Au–Pt heterodimers with smaller Au sizes exhibit broadened plasmon bands of reduced intensity.

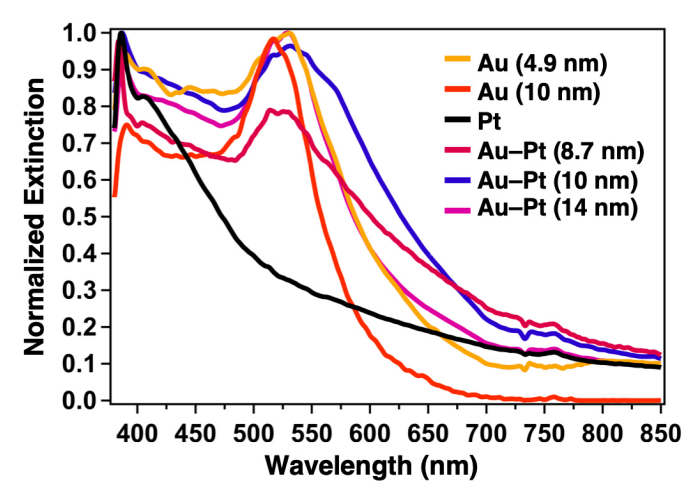


Figure 4: Steady-state extinction spectra of Au nanoparticles, Pt nanoparticles, and Au–Pt heterodimers dispersed in toluene.

Femtosecond Electron Dynamics of Au–Pt Heterodimers

In order to study the size-dependent electronic properties of Au–Pt heterodimers, we conducted femtosecond time-resolved transient absorption (TA) measurements. The excitation and detection pulses were tuned to the maximum frequency of the LSPR for each sample (530 nm).

We focus on the quantification of τ_{e-ph}, the electron-phonon coupling time constant, in the Au–Pt heterodimers, where the size of the Au domain was varied across each sample while the Pt domain size was held constant. Figures 5A and 5B display false-color transient absorption maps, where the TA signal magnitude obtained at multiple probe wavelengths is plotted vs. the pump-probe time delay. Time-dependent TA signal magnitudes obtained at select probe wavelengths of colloidal Au nanoparticles and Au-Pt heterodimers are shown in Figure 5C. The time dependence of the TA signal of the Au-Pt sample having a 14 nm Au domain size is compared for several excitation powers in Figure 5D. The power dependence of the data shown in Figure 5D were general across all of the nanoparticle systems studied. The TA maps qualitatively illustrate the ultrafast electronic relaxation dynamics by monitoring the recovery of the ground state bleach of Au-Pt heterodimers having 14 nm Au domains (Figures 5A and S9A) and the 4.9 nm Au nanoparticles (Figures 5B and S9B). The transient bleach magnitude recovers as the system equilibrates through electron-phonon scattering and energy dissipation to the surroundings. These processes are quantified by plotting the time-dependent amplitude at a specific wavelength against pump-probe delay time and fitting the data with an exponential function convoluted with the instrument response. As shown in Figure 5C, and consistent with previous experiments, there is no significant difference in τ_{e-ph} between Au (4.9 nm) and Au (10 nm) nanoparticles; the electron-phonon coupling rates of the Au nanoparticles by themselves is independent of size in the range studied. This result on the Au nanoparticle control samples was expected, because Au nanoparticles in this size range are known to exhibit size-independent electron-phonon coupling rates.33,34

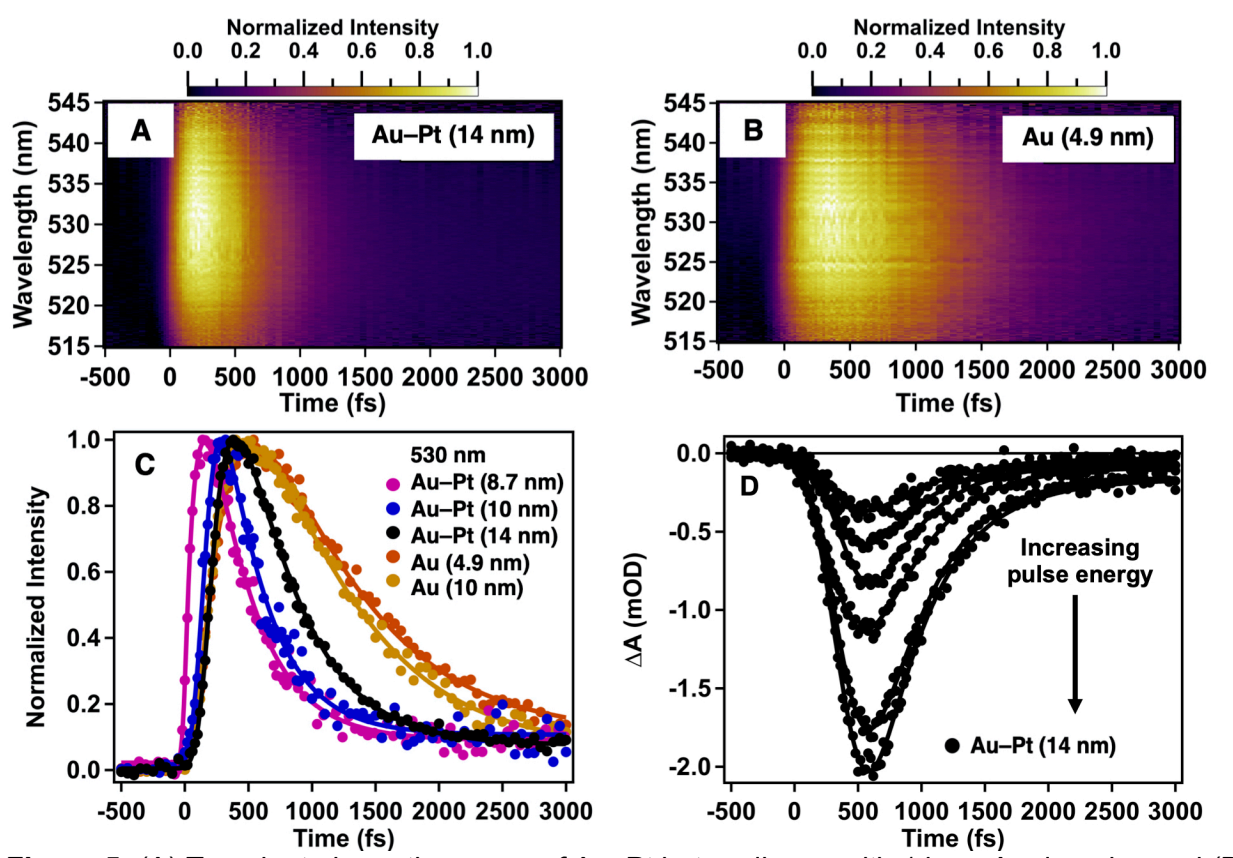


Figure 5: (A) Transient absorption maps of Au–Pt heterodimers with 14 nm Au domains and (B) 4.9 nm Au nanoparticles. Time-dependent dynamics of various Au–Pt heterodimers and Au nanoparticles and pump power dependent traces of Au–Pt heterodimers with 14 nm Au domains are shown in (C) and (D), respectively.

An important observation from these experiments is that all of the Au–Pt heterodimers exhibit significantly faster decay times than that of pure Au nanoparticles (Figure 5C). Qualitatively, these results indicate that incorporation of the Pt domain causes more rapid conversion of the hot electron population to local heating of the lattice. Moreover, these decay time constants also vary significantly within the Au–Pt heterodimer series. In order to understand the composition-dependent time-domain results shown in Figure 5C, the power dependence of the electron-phonon relaxation rates was quantified using the two-temperature model (TTM) of an electron gas. Initially, a hot Fermi-Dirac distribution is generated through electron-electron scattering. The metal lattice remains at laboratory temperature, due to the selective excitation of the conduction band electrons. Subsequently, these photo-excited electrons will relax by electron-phonon scattering with the vibrational modes of the lower-temperature lattice. The resultant electron-phonon coupling rates depend primarily on the non-equilibrium electron temperature and the nanoparticle electron-phonon coupling constant, g. This relationship is described by the following pair of differential equations:

$$C_e(T_e)\frac{\partial T_e}{\partial t} = -g(T_e - T_l),$$

$$C_l\frac{\partial T_l}{\partial t} = g(T_e - T_l),$$

where $C_e = \gamma T_e$ is the temperature-dependent electron heat capacity, γ is the bulk electron-phonon coupling constant for Au (66 J m⁻³ K⁻²),³⁶ C_l is the lattice heat capacity, T_e and T_l are the electron and lattice temperatures, respectively, and g is the electron-phonon coupling constant.

Importantly, the material electron-phonon coupling constant can be determined by analyzing the electron-phonon relaxation time constants as a linear function of the instantaneous electron temperature. This is true because in the low perturbation regime, the instantaneous electron temperature scales linearly with the pump pulse energy, which is controlled in the laboratory. We note that this model is valid throughout the electronic excitation spectrum; the electron-phonon scattering rate is not sensitive to interband or intraband excitation. Thus, we performed pump-pulse energy dependent TA studies to elucidate the influence of nanostructure composition on the electron-phonon coupling constant. A typical response is illustrated in Figure 5D, which shows time-dependent TA traces of Au–Pt heterodimers having 14 nm Au domains at different pump pulse energies. The pulse-energy-dependent τ_{e-ph} time constants for all Au nanoparticles and Au–Pt heterodimers studied are summarized in Figure 6A. As the data in Figure 6A reveal, the τ_{e-ph} values varied systematically across the Au–Pt series.

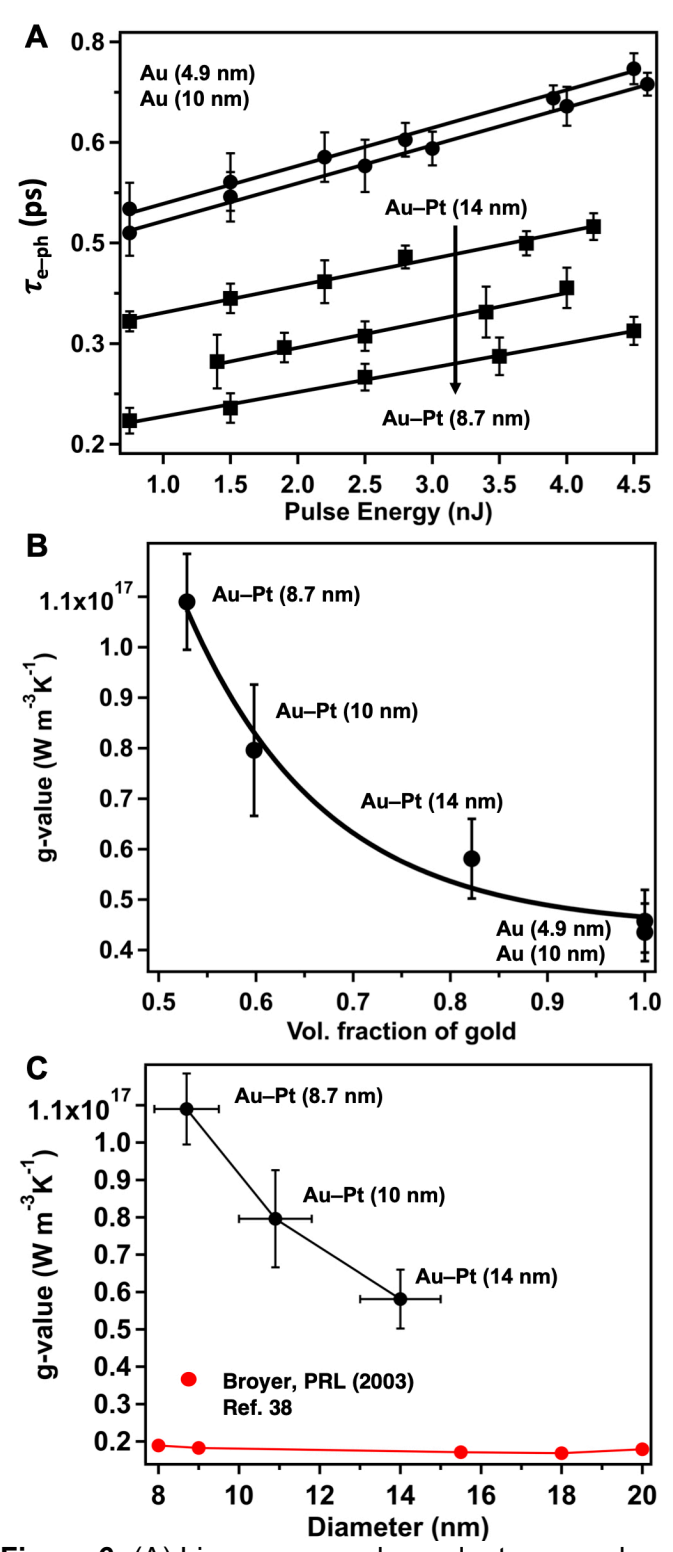


Figure 6: (A) Linear energy dependent τ_{e-ph} values for all samples following the two-temperature model (TTM). (B) Resultant g-values plotted against the volume fraction of Au for Au–Pt heterodimers and Au nanoparticles. The solid line represents an exponential fit. This suggests that electron-phonon coupling follows a more Boltzmann-like distribution and is not simply dependent on the mole fraction ratio of Au:Pt. (C) Resulting g-values plotted against

nanoparticle diameter for both Au–Pt heterodimers and gold nanoparticles. The values for Au nanoparticles (red) were obtained from reference 38.

Using the data in Figure 6A, the intrinsic electron-phonon coupling constant, g, for each system was determined by extrapolation of the rate constants to zero pump pulse energy, which represents the laboratory temperature, (T^0).

$$\tau_{e-ph}^0 = \frac{\gamma T^0}{g}$$

The laboratory-temperature electron-phonon coupling constant, τ_{e-ph}^0 , is inversely related to the material electron-phonon constant through \mathcal{T}^0 and γ . The resultant g values scale exponentially with Au volume fraction across the Au–Pt samples studied (Figure 6B).

The volume-dependent g values of the Au-Pt heterodimers can be understood by considering the density of available electronic states (DOS) near the Fermi-level. This DOS is expected to play a role in determining τ_{e-nh}^0 because the Fermi-level in Pt resides at the high-energy side of a mostly filled d-band.³⁷ This electronic configuration is opposite of that for most coinage metals (Ag, Au, and Cu), where the Fermi-level has minimal overlap with the filled d-band. Hartland et al. investigated the electron-phonon dynamics of Pt@Au core@shell nanoparticles and also observed faster τ_{e-ph} for the bimetallic systems. 9 The authors modeled the dynamics of Pt@Au nanoparticles using a first-order rate model that assumes relaxation is dependent on the number of available electronic states at the Fermi-level. Further, they observed that τ_{e-ph} varied little with the thickness of the Au shell. These results suggest that Pt dominated the relaxation dynamics, even at Pt:Au molar ratios of 1:6. We extend this model to our results, by comparing the effective electron-phonon coupling constant to the volume fraction of Au for each of the three Au-Pt heterodimers using size parameters obtained from TEM images in Figure 1. Figure 6B shows the respective g values plotted against the volume fraction of Au. The observed trend was accurately described using a single-exponential fit function, which was characteristic of a Boltzmann distribution of energy levels. Hence, the structure-dependent electron-phonon coupling rates scale monotonically with Au volume fraction, and result from systematic differences in the DOS near the Au Fermi-level.

Specifically, interfacing smaller Au domains on the surface edges of Pt nanocubes causes an increase in the density of states about the Fermi-level of Au. This resulted in accelerated thermalization times through an increased number of electron-phonon interactions. Hence. synthetic control over the composition and sizes of the domains in hybrid nanoparticles can be used to manipulate the physical and electronic properties of these materials. The results in Figure 6C compare the size-dependent electron-phonon coupling constants for Au-Pt observed in this work to that of gold nanospheres obtained previously. 38 The data clearly demonstrate that the extent of the electron-phonon scattering size dependence is much larger for the Au-Pt systems than for Au nanospheres. We also note that although Au nanospheres with diameters less than approximately 5 nm exhibit size-dependent electron-phonon scattering rates, this effect saturates for larger sizes and is size independent in the range of diameters (8 nm - 20 nm) considered here.³⁸ In a separate but related study, size-dependent changes in electronphonon coupling constants for Au nanospheres spanning 2 nm to 8 nm diameter were concluded to be smaller than experimental error.³³ We do note that although absolute determinations of material g factors obtained from different laser systems can vary slightly, the results on Au nanospheres presented here are in general agreement, and point to the size

independence of electron-phonon coupling constants in the range of interest. This lack of size dependence for Au nanoparticle electron-phonon coupling is attributed to Au domains – even for the small domain sizes considered here – adopting bulk-like phonon scattering properties. In contrast, increasing the Au domain diameter of the Au-Pt systems by approximately 50% results in a greater than 80% reduction of the material electron-phonon coupling constant (Figure 6C). Hence, we attribute the observed size-dependent electronic relaxation dynamics to synergistic properties of the Au-Pt system. Specifically, interfacing Au with Pt results in an increased density of states near the Au Fermi level. 37 This effect stems from the Pt Fermi level coinciding with the high-energy portion of the metal d band. The increased density of states is expected to exhibit increased electron-phonon scattering rates, resulting in the size-dependent a values reported in Figure 6. An important distinction between our results and those from previous research on Au@Pt and Pt@Au nanoparticles is the observation of volume-dependent Au relaxation rates. Given that even the smallest Au nanoparticles adopt bulk-like electronphonon scattering properties,³³ the accelerated thermalization observed here can be attributed to an increased carrier density resulting from the incorporation of the Pt domain. We note that structure-dependent influences on rapid electron-surface scattering are not expected to affect the electron-phonon coupling rates, which occur on longer timescales of several hundreds of femtoseconds. The ability to fine tune the electron-phonon coupling properties of metallic nanostructures, and observe these effects experimentally, is a direct result of the nanostructural control afforded by the synthetic methodology. The formation of multi-component nanostructures with a high degree of size and morphology control may enable additional insights into how morphology, composition, and interfacial structure influence the physical and electronic properties of metallic materials.

CONCLUSIONS

We have systematically tuned the Au domain size of Au–Pt hybrid nanoparticles from 4.4 to 16 nm, while keeping the size of the Pt domain constant, by changing both Au reagent concentration and reaction time. This allowed us to interrogate the size-dependent electron-phonon relaxation rates of Au nanoparticles bound to Pt. For a fixed Pt domain size, increasing the Au diameter from 8.7 nm to 14 nm decreased the material's electron-phonon coupling constant by more than 80%, which is not possible for comparably sized Au nanoparticles. The incorporation of the Pt domain circumvented the bulk-like limit for electronic electron thermalization imposed on even small Au nanoparticles. The observation that the electron-phonon relaxation rates of the Au–Pt heterodimers are dependent upon the size of the Au domain is significant, because the relaxation rates of Au nanoparticles by themselves are not size dependent in the range studied. Hence, the Au–Pt heterostructure platform provides an opportunity to achieve electronic and energy management capabilities that are not possible for isolated Au nanoparticles. This has important implications for the design and synthesis of composite materials for photocatalytic and light-harvesting applications, as well as the use of colloidal hybrid nanoparticles to engineer different functions into established materials.

EXPERIMENTAL SECTION

Materials. Octadecene [ODE, 90%, technical grade], oleylamine [OLAM, 70%, technical grade], oleic acid [OLAC, 90%, technical grade], platinum(II) acetylacetonate [Pt(acac)₂, ≥99.98% trace metals basis], gold(III) chloride hydrate [HAuCl₄·xH₂O, 99.995% trace metals basis], and iron(0) pentacarbonyl [Fe(CO)₅, >99.99% trace metals basis] were purchased from Sigma-Aldrich. All

solvents, including hexanes [mixture of isomers], toluene, acetone, and isopropanol [IPA] were of analytical grade. All chemicals were used as received without further purification.

Synthesis of Pt nanoparticles. Pt nanoparticles were prepared using a modification of a published procedure.³⁰ Briefly, Pt(acac)₂ (200 mg), ODE (20 mL), OLAC (2 mL), and OLAM (2 mL) were combined in a 50 mL 3-neck round bottom flask equipped with a reflux condenser. gas flow adapter, alcohol thermometer, rubber septum, and magnetic stir bar. The mixture was placed under vacuum, heated to 110 °C, and maintained for 30 minutes. The flask was then placed under an Ar blanket after cycling between Ar and vacuum three times, and heated to 180 °C, when 200 μL of a solution of Fe(CO)₅ (200 μL) and ODE (1.8 mL) was rapidly injected. The flask was then heated to 190 °C and the reaction was allowed to proceed for 60 minutes. The reaction was then removed from heat and cooled to room temperature. The product was isolated by addition of acetone into the reaction mixture followed by centrifugation and resuspension in hexanes. The centrifugation/resuspension process was repeated twice more. with the addition of a few drops of OLAM in the final centrifugation step, and the final product resuspended in 5 mL of hexanes for characterization and use in further reactions. Nanoparticles used for transient absorption spectroscopy were dried out of suspension and redispersed in toluene. Statistical measurements of 150 nanoparticles were taken along both the length and width of the Pt nanocubes.

Synthesis of Au-Pt hybrid nanoparticles. Au-Pt hybrid nanoparticles were prepared using a modification of published procedures.^{28,29} Briefly, HAuCl₄·xH₂O, hexanes (0.5 mL), OLAM (0.5 mL), ODE (5 mL), and Pt seeds (10 mg) in hexanes were combined in a 50 mL 3-neck round bottom flask equipped with a reflux condenser, gas flow adapter, thermocouple, rubber septum. and magnetic stir bar. The concentrations of HAuCl₄·xH₂O (and corresponding mg of HAuCl₄·xH₂O in parentheses) used to make the various Au−Pt hybrid nanoparticles were 3.4 mM (8.0 mg), 6.1 mM (14.5 mg), 8.5 mM (20.0 mg), 11.8 mM (28.0 mg), 22.0 mM (52.0 mg), and 37.2 mM (88.0 mg); more details are provided in Table S1 of the Supporting Information. Additionally, time studies were carried out for the sample that used 11.8 mM (28.0 mg) HAuCl₄·xH₂O by taking aliquots at 0, 1.5, 5, 15, 30, 45, 60, 90, 120, and 240 min; more details are provided in Table S2 of the Supporting Information. For all reactions, the mixture was placed under vacuum at room temperature for 30 seconds, after which the flask was placed under an Ar blanket and heated to 80 °C. The reaction was then allowed to proceed at 80 °C for 4 hours. The reaction was then removed from heat and cooled to room temperature. The product was isolated by addition of IPA into the reaction mixture followed by centrifugation and resuspension in hexanes. The centrifugation/resuspension process was repeated twice more, with the addition of a few drops of OLAM in the final centrifugation step, and the final product resuspended in 5 mL of hexanes for characterization and use in further reactions. Nanoparticles used for ultrafast transient absorption experiments were dried out of suspension and redispersed in toluene. Statistical measurements of 150 nanoparticles were taken along the diameter of the spherical Au domain, parallel to the interface with the cubic Pt domain.

Synthesis of 5 nm Au nanoparticles. Au nanoparticles with a diameter of 5 nm were prepared using a modification of a published procedure. ¹⁶ Briefly, $HAuCl_4 \cdot xH_2O$ (100 mg), toluene (8 mL), and 70% OLAM (8 mL) were added to a 40 mL scintillation vial and stirred under ambient conditions. In a second vial, borane tert-butylamine (50 mg) was dissolved in OLAM (1 mL) and toluene (1 mL). This solution was then injected into the gold precursor solution and allowed to stir for 45 minutes under ambient conditions. The product was isolated by addition of EtOH into the reaction mixture followed by centrifugation and resuspension in hexanes. The centrifugation/resuspension process was repeated twice more, with the addition of a few drops of OLAM in the final centrifugation step, and the final product was resuspended in 5 mL of

hexanes for characterization and use in further reactions. Statistical measurements of 150 nanoparticles were taken along the diameter of the spherical Au nanoparticles.

Synthesis of 10 nm Au nanoparticles. Au nanoparticles with a diameter of approximately 10 nm were prepared using a modification of a published procedure. Briefly, HAuCl₄·xH₂O (100 mg), OLAM (10 mL), and toluene (10 mL) were combined in a 50 mL 3-neck round bottom flask equipped with a reflux condenser, gas flow adapter, thermocouple, rubber septum, and magnetic stir bar. The mixture was placed under Ar flow until it reached approximately 60 °C, after which it was placed under an Ar blanket, heated to 120 °C, and maintained for 45 minutes. The reaction was then removed from the heat and cooled to room temperature. The product was isolated by addition of EtOH into the reaction mixture followed by centrifugation and resuspension in hexanes. The centrifugation/resuspension process was repeated twice more, with the addition of a few drops of OLAM in the final centrifugation step, and the final product resuspended in 5 mL of hexanes for characterization and use in further reactions. Statistical measurements of 150 nanoparticles were taken along the diameter of the spherical Au nanoparticles.

Nanoparticle characterization. Transmission electron microscopy (TEM) images were collected on a FEI Tecnai G2 XTWIN with a LaB₆ source operating at 200 kV. ImageJ software³⁹ was used in the statistical measurements of nanoparticle TEM images. High angle annular dark field scanning TEM (HAADF-STEM) and STEM energy dispersive X-ray spectroscopy (STEM-EDS) element maps were collected on a FEI Talos F200X S/TEM at an accelerating voltage of 200 kV. Standardless Cliff-Lorimer quantification, with QMAP resolution, was performed on the deconvoluted EDS line intensity data using the Bruker Espirit software. ES vision software (Emispec) was used for EDS data processing. EDS lines for each element map shown in the paper are Pt Lα and Au Lβ. Samples for TEM analysis were all drop-casted onto 400-mesh nickel TEM grids with a carbon/formvar film. Powder X-ray diffraction (XRD) data were collected on a Bruker D-8 Advance X-ray Diffractometer using Cu Kα radiation. CrystalMaker and CrystalDiffract software was used to simulate crystal structures and diffraction patterns. MATLAB software was used to generate all plots in this publication (*MATLAB ver. R2020a*).

Optical absorption characterization. The UV-Vis extinction spectra of each sample were collected in quartz cuvettes with a 0.2 cm pathlength after dispersion in toluene. The spectra were acquired using a Pasco Vis Spectrometer equipped with a tungsten lamp and 2-3 nm Full-Width Half-Maximum (FWHM) spectral resolution. The traces in Figure 4 were normalized to the maximum absorption intensity for each trace.

Ultrafast Transient Absorption Experiments. Transient absorption instrumentation was used as previously reported.⁴¹ A noncollinear optical parametric amplifier (NOPA) was used to generate pump and probe pulses centered at the LSPR wavelength of 530 nm, with a FWHM of 23 nm, which equates to a transform limited pulse duration of 19 fs. The spot size of the pump/probe pulses are approximately 1.6 and 1.3 μm, respectively. The probe pulse was attenuated to 0.4 nJ/pulse for all transient absorption experiments. The NOPA was seeded by the 1040 nm fundamental from an ytterbium amplifier (Spirit, Spectra-Physics) modulated at a repetition rate of 100 kHz. The NOPA output beam was compressed using dispersion-compensating mirrors (DCM) then directed to the 2DQuickVisible setup (PhaseTech) and split using a 90/10 beam splitter. The 90% transmitted beam provided the pump pulse that was temporally delayed using a mechanical delay stage. The pump pulse was focused and spatially overlapped with the probe pulse at the sample. The transmitted probe pulse was dispersed on a SP2150i array detector (Princeton Instruments).

ASSOCIATED CONTENT

Supporting Information. The Supporting Information is available free of charge at (insert link).

 Additional characterization data, including XRD and EDS spectra, and tables of experimental data, including precursor concentrations and aliquot removal times.

AUTHOR INFORMATION

Corresponding Authors

- * R. E. Schaak. Email: res20@psu.edu
- * K. L. Knappenberger, Jr. Email: klk260@psu.edu

Notes

The authors declare no competing financial interest.

ACKNOWLEDGEMENTS

This work was supported by the U.S. National Science Foundation under grants CHE-1707830 (A.M.F., R.E.S.) and CHE-1807999 (W.R.J., K.L.K.) and the Air Force Office of Scientific Research under Grant FA9550-18-1-0347 (W.R.J., K.L.K.). Electron microscopy was performed at the Materials Characterization Lab of the Penn State Materials Research Institute. The authors would like to thank Emil A. Hernandez-Pagan and Benjamin C. Steimle for insightful discussions.

REFERENCES

- (1) Buck, M. R.; Bondi, J. F.; Schaak, R. E. A Total-Synthesis Framework for the Construction of High-Order Colloidal Hybrid Nanoparticles. *Nat. Chem.* **2012**, *4*, 37–44. https://doi.org/10.1038/nchem.1195.
- (2) Banin, U.; Ben-Shahar, Y.; Vinokurov, K. Hybrid Semiconductor–Metal Nanoparticles: From Architecture to Function. *Chem. Mater.* **2014**, *26*, 97–110. https://doi.org/10.1021/cm402131n.
- (3) Davide Cozzoli, P.; Pellegrino, T.; Manna, L. Synthesis, Properties and Perspectives of Hybrid Nanocrystal Structures. *Chem. Soc. Rev.* **2006**, *35*, 1195–1208. https://doi.org/10.1039/B517790C.
- (4) Schick, I.; Lorenz, S.; Gehrig, D.; Schilmann, A.-M.; Bauer, H.; Panthöfer, M.; Fischer, K.; Strand, D.; Laquai, F.; Tremel, W. Multifunctional Two-Photon Active Silica-Coated Au@MnO Janus Particles for Selective Dual Functionalization and Imaging. *J. Am. Chem. Soc.* **2014**, *136*, 2473–2483. https://doi.org/10.1021/ja410787u.
- (5) Cushing, S. K.; Li, J.; Meng, F.; Senty, T. R.; Suri, S.; Zhi, M.; Li, M.; Bristow, A. D.; Wu, N. Photocatalytic Activity Enhanced by Plasmonic Resonant Energy Transfer from Metal to Semiconductor. *J. Am. Chem. Soc.* 2012, 134, 15033–15041. https://doi.org/10.1021/ja305603t.
- (6) Furube, A.; Du, L.; Hara, K.; Katoh, R.; Tachiya, M. Ultrafast Plasmon-Induced Electron Transfer from Gold Nanodots into TiO₂ Nanoparticles. *J. Am. Chem. Soc.* **2007**, *129*, 14852–14853. https://doi.org/10.1021/ja076134v.

- (7) Wu, K.; Rodríguez-Córdoba, W. E.; Yang, Y.; Lian, T. Plasmon-Induced Hot Electron Transfer from the Au Tip to CdS Rod in CdS-Au Nanoheterostructures. *Nano Lett.* **2013**, 13, 5255–5263. https://doi.org/10.1021/nl402730m.
- (8) Engelbrekt, C.; Crampton, K. T.; Fishman, D. A.; Law, M.; Apkarian, V. A. Efficient Plasmon-Mediated Energy Funneling to the Surface of Au@Pt Core–Shell Nanocrystals. *ACS Nano* **2020**, *14*, 5061–5074. https://doi.org/10.1021/acsnano.0c01653.
- (9) Hodak, J. H.; Henglein, A.; Hartland, G. V. Tuning the Spectral and Temporal Response in PtAu Core–Shell Nanoparticles. *J. Chem. Phys.* **2001**, *114*, 2760–2765. https://doi.org/10.1063/1.1339266.
- (10) Jana, N. R.; Gearheart, L.; Murphy, C. J. Seeding Growth for Size Control of 5–40 nm Diameter Gold Nanoparticles. *Langmuir* **2001**, *17*, 6782–6786. https://doi.org/10.1021/la0104323.
- (11) Sau, T. K.; Murphy, C. J. Room Temperature, High-Yield Synthesis of Multiple Shapes of Gold Nanoparticles in Aqueous Solution. *J. Am. Chem. Soc.* **2004**, *126*, 8648–8649. https://doi.org/10.1021/ja047846d.
- (12) Yu, H.; Chen, M.; Rice, P. M.; Wang, S. X.; White, R. L.; Sun, S. Dumbbell-Like Bifunctional Au–Fe₃O₄ Nanoparticles. *Nano Lett.* **2005**, *5*, 379–382. https://doi.org/10.1021/nl047955q.
- (13) Read, C. G.; Biacchi, A. J.; Schaak, R. E. Au–Ge and Ag–Ge Heterodimers with Tunable Domain Sizes: A Supersaturation-Precipitation Route to Colloidal Hybrid Nanoparticles. *Chem. Mater.* **2013**, *25*, 4304–4311. https://doi.org/10.1021/cm4024452.
- (14) Gordon, T. R.; Schaak, R. E. Synthesis of Hybrid Au-In₂O₃ Nanoparticles Exhibiting Dual Plasmonic Resonance. *Chem. Mater.* **2014**, *26*, 5900–5904. https://doi.org/10.1021/cm502396d.
- (15) Sanchez, A.; Abbet, S.; Heiz, U.; Schneider, W.-D.; Häkkinen, H.; Barnett, R. N.; Landman, U. When Gold Is Not Noble: Nanoscale Gold Catalysts. *J. Phys. Chem. A* **1999**, *103*, 9573–9578. https://doi.org/10.1021/jp9935992.
- (16) Peng, S.; Lee, Y.; Wang, C.; Yin, H.; Dai, S.; Sun, S. A Facile Synthesis of Monodisperse Au Nanoparticles and Their Catalysis of CO Oxidation. *Nano Res.* **2008**, *1*, 229–234. https://doi.org/10.1007/s12274-008-8026-3.
- (17) Wang, C.; Yin, H.; Dai, S.; Sun, S. A General Approach to Noble Metal–Metal Oxide Dumbbell Nanoparticles and Their Catalytic Application for CO Oxidation. *Chem. Mater.* **2010**, *22*, 3277–3282. https://doi.org/10.1021/cm100603r.
- (18) Valden, M.; Lai, X.; Goodman, D. W. Onset of Catalytic Activity of Gold Clusters on Titania with the Appearance of Nonmetallic Properties. *Science* **1998**, *281*, 1647–1650. https://doi.org/10.1126/science.281.5383.1647.
- (19) Lee, H.-E.; Yang, K. D.; Yoon, S. M.; Ahn, H.-Y.; Lee, Y. Y.; Chang, H.; Jeong, D. H.; Lee, Y.-S.; Kim, M. Y.; Nam, K. T. Concave Rhombic Dodecahedral Au Nanocatalyst with Multiple High-Index Facets for CO₂ Reduction. *ACS Nano* **2015**, *9*, 8384–8393. https://doi.org/10.1021/acsnano.5b03065.
- (20) Lv, H.; Xi, Z.; Chen, Z.; Guo, S.; Yu, Y.; Zhu, W.; Li, Q.; Zhang, X.; Pan, M.; Lu, G.; Mu, S.; Sun, S. A New Core/Shell NiAu/Au Nanoparticle Catalyst with Pt-Like Activity for Hydrogen Evolution Reaction. *J. Am. Chem. Soc.* **2015**, *137*, 5859–5862. https://doi.org/10.1021/jacs.5b01100.
- (21) Lee, Y.; Garcia, M. A.; Frey Huls, N. A.; Sun, S. Synthetic Tuning of the Catalytic Properties of Au-Fe₃O₄ Nanoparticles. *Angew. Chem.* **2010**, *122*, 1293–1296. https://doi.org/10.1002/ange.200906130.
- (22) Hartland, G. V. Optical Studies of Dynamics in Noble Metal Nanostructures. *Chem. Rev.* **2011**, *111*, 3858–3887. https://doi.org/10.1021/cr1002547.

- (23) Zhang, Y.; He, S.; Guo, W.; Hu, Y.; Huang, J.; Mulcahy, J. R.; Wei, W. D. Surface-Plasmon-Driven Hot Electron Photochemistry. *Chem. Rev.* **2018**, *118*, 2927–2954. https://doi.org/10.1021/acs.chemrev.7b00430.
- (24) Jain, P. K.; Huang, X.; El-Sayed, I. H.; El-Sayed, M. A. Noble Metals on the Nanoscale: Optical and Photothermal Properties and Some Applications in Imaging, Sensing, Biology, and Medicine. *Acc. Chem. Res.* **2008**, *41*, 1578–1586. https://doi.org/10.1021/ar7002804.
- (25) Kristian, N.; Wang, X. Pt_{shell}–Au_{core}/C Electrocatalyst with a Controlled Shell Thickness and Improved Pt Utilization for Fuel Cell Reactions. *Electrochem. Commun.* **2008**, *10*, 12–15. https://doi.org/10.1016/j.elecom.2007.10.011.
- (26) Habas, S. E.; Lee, H.; Radmilovic, V.; Somorjai, G. A.; Yang, P. Shaping Binary Metal Nanocrystals through Epitaxial Seeded Growth. *Nat. Mater.* **2007**, *6*, 692–697. https://doi.org/10.1038/nmat1957.
- (27) Lim, S. I.; Varon, M.; Ojea-Jiménez, I.; Arbiol, J.; Puntes, V. Pt Nanocrystal Evolution in the Presence of Au(III)-Salts at Room Temperature: Spontaneous Formation of AuPt Heterodimers. *J. Mater. Chem.* **2011**, *21*, 11518–11523. https://doi.org/10.1039/C1JM10313J.
- (28) Bradley, M. J.; Read, C. G.; Schaak, R. E. Pt–Au Nanoparticle Heterodimers as Seeds for Pt–Au–Metal Sulfide Heterotrimers: Thermal Stability and Chemoselective Growth Characteristics. *J. Phys. Chem. C* **2015**, *119*, 8952–8959. https://doi.org/10.1021/acs.jpcc.5b01274.
- (29) Wang, C.; Tian, W.; Ding, Y.; Ma, Y.; Wang, Z. L.; Markovic, N. M.; Stamenkovic, V. R.; Daimon, H.; Sun, S. Rational Synthesis of Heterostructured Nanoparticles with Morphology Control. *J. Am. Chem. Soc.* **2010**, *132*, 6524–6529. https://doi.org/10.1021/ja101305x.
- (30) Hodges, J. M.; Morse, J. R.; Fenton, J. L.; Ackerman, J. D.; Alameda, L. T.; Schaak, R. E. Insights into the Seeded-Growth Synthesis of Colloidal Hybrid Nanoparticles. *Chem. Mater.* **2017**, *29*, 106–119. https://doi.org/10.1021/acs.chemmater.6b02795.
- (31) Henglein, A. Preparation and Optical Aborption Spectra of Au_{core}Pt_{shell} and Pt_{core}Au_{shell} Colloidal Nanoparticles in Aqueous Solution. *J. Phys. Chem. B* **2000**, *104*, 2201–2203. https://doi.org/10.1021/jp994300i.
- (32) Ma, H.; Liu, X.; Gao, C.; Yin, Y. The Calculated Dielectric Function and Optical Properties of Bimetallic Alloy Nanoparticles. *J. Phys. Chem. C* **2020**, *124*, 2721–2727. https://doi.org/10.1021/acs.jpcc.9b11154.
- (33) Hodak, J. H.; Henglein, A.; Hartland, G. V. Electron-Phonon Coupling Dynamics in Very Small (Between 2 and 8 nm Diameter) Au Nanoparticles. *J. Chem. Phys.* **2000**, *112*, 5942–5947. https://doi.org/10.1063/1.481167.
- (34) Link, S.; Burda, C.; Wang, Z. L.; El-Sayed, M. A. Electron Dynamics in Gold and Gold–Silver Alloy Nanoparticles: The Influence of a Nonequilibrium Electron Distribution and the Size Dependence of the Electron–Phonon Relaxation. *J. Chem. Phys.* 1999, 111, 1255–1264. https://doi.org/10.1063/1.479310.
- (35) Kaganov, M. I.; Lifshitz, I. M.; Tanatarov, L. V. Relaxation Between Electrons and the Crystalline Lattice. *Sov. Phys. JETP*, **1957**, *4*, 173–178.
- (36) Hodak, J. H.; Martini, I.; Hartland, G. V. Spectroscopy and Dynamics of Nanometer-Sized Noble Metal Particles. J. Phys. Chem. B 1998, 102, 6958–6967. https://doi.org/10.1021/jp9809787.
- (37) Lin, Z.; Zhigilei, L. V.; Celli, V. Electron-Phonon Coupling and Electron Heat Capacity of Metals under Conditions of Strong Electron-Phonon Nonequilibrium. *Phys. Rev. B* **2008**, 77, 075133. https://doi.org/10.1103/PhysRevB.77.075133.
- (38) Arbouet, A.; Voisin, C.; Christofilos, D.; Langot, P.; Fatti, N. D.; Vallée, F.; Lermé, J.; Celep, G.; Cottancin, E.; Gaudry, M.; Pellarin, M.; Broyer, M.; Maillard, M.; Pileni, M. P.;

- Treguer, M. Electron-Phonon Scattering in Metal Clusters. *Phys. Rev. Lett.* **2003**, *90*, 177401. https://doi.org/10.1103/PhysRevLett.90.177401.
- (39) Rasband, W. S. *ImageJ*; U. S. National Institutes of Health: Bethesda, Maryland, 1997.
- (40) Palmer, D. C. CrystalMaker, CrystalMaker Software Ltd.: Oxfordshire, England, 2014.
- (41) Jeffries, W. R.; Park, K.; Vaia, R. A.; Knappenberger, K. L. Resolving Electron–Electron Scattering in Plasmonic Nanorod Ensembles Using Two-Dimensional Electronic Spectroscopy. *Nano Lett.* **2020**, *20*, 7722–7727. https://doi.org/10.1021/acs.nanolett.0c03272.

Table of Contents Graphic

